

The effect of viscoelasticity on stress fields within polyethylene melt flow for a cross-slot and contraction–expansion slit geometry

D. G. Hassell · D. Auhl · T. C. B. McLeish · Malcolm R. Mackley

Received: 12 October 2007 / Revised: 17 January 2008 / Accepted: 19 January 2008 / Published online: 13 February 2008
© Springer-Verlag 2008

Abstract The sensitivity of the principal stress difference (PSD) profiles to material viscoelasticity is demonstrated for two flow geometries using three different polyethylenes. Studies were performed using both experimental optical techniques and computational simulations, in the latter case to evaluate the ability to model these complex flows. The materials were characterised using linear and extensional rheology which was fitted to a multimode POM-POM model implemented in the Lagrangian–Eulerian code *flowSolve*. A contraction–expansion (CE) slit geometry was used to create a mixed, but primarily simple shear flow, whilst a cross-slot geometry provided a region of high extensional shear and high strain. In both flows, the PSD developed from an initial Newtonian profile to increasing levels of asymmetry between the inlet and the outlet flow. More specific phenomena, such as downstream stress fangs in the CE slit and the formation of centreline cusps and “W”-shaped cusps in the cross-slot, were also observed. The simulations of PSD development within the CE slit geometry quantitatively captured the experimental results. In the case of the cross-slot geometry, the qualitative features of the PSD development were well captured, although the results were quantitatively less accurate.

Keywords Viscoelastic fluid · Flow modeling · Polyethylene · Birefringence

Introduction

Recent developments in rheology characterisation, molecular-based rheological models, numerical simulation and precise polymer processing now make it possible to rank numerical prediction of a polymer process with experimental observations. Published work has compared a number of operating parameters, including pressure drop (Collis and Mackley 2005; Valette et al. 2006), flow-induced birefringence (Lee et al. 2001; Agassant et al. 2002; Clemeur et al. 2004a; Soulages 2007) and velocity fields (Peters et al. 1999; Mitsoulis et al. 2003; Sirakov et al. 2005) for flow fields exhibiting both regions of simple shear and extensional flow. In each case, different polymers, geometries, models and codes have been used, and, in general, reasonable success has been reported in the matching of simulation with experiment.

In this paper, experimental results for both a contraction–expansion (CE) slit and a cross-slot geometry are reported. These experiments were carried out using a Cambridge multi-pass rheometer (MPR; see for instance Mackley et al. 1995), and this enabled small quantities of polymer to be tested with precision. This CE slit creates regions of high simple shear near to the slit walls and extensional flow in the region of the symmetry line in the inlet and outlet areas of the flow. Conventional simple shear flow is commonly produced using either parallel plate, sliding plate or cone and plate geometries (see for instance Wagner et al. 2005). For complex flows that mimic more closely industrial applications, such as polymer extrusion, the use of a straight channel or contraction expansion slit geometry

D. G. Hassell · M. R. Mackley (✉)
Department of Chemical Engineering, University of Cambridge,
Pembroke Street,
Cambridge CB2 3RA, UK
e-mail: mrm1@cheng.cam.ac.uk

D. G. Hassell
e-mail: dgh33@cam.ac.uk

D. Auhl · T. C. B. McLeish
IRC in Polymer Science and Technology,
Department of Physics and Astronomy, University of Leeds,
Leeds LS2 9JT, UK

provides regions of high simple shear near the wall. These types of flow have been used for many years to identify the flow behaviour of polymer melts (see for instance Han and Drexler 1973; Han 1976; Checker et al. 1983) and to investigate the differences in material behaviour (see for instance Beraudo et al. 1998).

The cross-slot is a more recent geometry used for polymer melt and solution studies and creates a region of high extensional deformation along the inlet–outlet symmetry plane. Simple strain extensional flow deformations are performed by stretching samples (Sridhar et al. 1991; Meissner and Hostettler 1994), whilst extension in complex flows is commonly generated around a stagnation point. Stagnation point flow was initially pioneered by G.I. Taylor in a four-roll mill (Taylor 1934). This technique was then extended to encompass both the two- (Frank and Mackley 1976) and four-roll mill (Crowley et al. 1976) for polymer solutions. A similar flow pattern is also generated using a cross-slot device (Scrivener et al. 1979), and the symmetry of this design provides very well-defined boundary conditions. Whilst the roll mill technique has been used for dilute polymer solutions, the cross-slot geometry has been applied for both solutions (Schoonen et al. 1998) and more recently to polymer melts using either large (Verbeeten 2001; Soulages et al. 2007) or small (Coventry and Mackley 2008) quantities of material.

Both the CE slit and cross-slot offer potential to explore the general processing behaviour of a viscoelastic melt within a complex flow. In this paper, three different polymers were chosen, exhibiting increasing levels of viscoelasticity, to characterise the effect of this increase on the stress present within polymer flow. The principal stress difference (PSD) was captured using flow birefringence and compared to simulation predictions. To match the experimental observation with simulations, it was necessary to characterise the flow behaviour of each polymer employing both linear oscillatory and transient rheological measurements. The rheological model chosen for fitting the experimental rheology and predicting the processing be-

haviour was the multimode POM-POM model (McLeish and Larson 1998; Blackwell et al. 2000). Numerical simulation of the complex flow was carried out using the Lagrangian–Eulerian finite element software *flowSolve* (Harlen et al. 1995). This provides a robust test of the models predictive performance for a range of flow rates within the two flow geometries, which exhibit different levels of simple shear and extensional flow.

Experimental

Materials characterisation

The materials used were three polyethylenes, the properties of which are outlined in Table 1. CM1 is a linear metallocene-catalysed polyethylene. HDB2 is a high-density branched polyethylene with long chain branches (Wood-Adams and Costeux 2001) which has been the subject of successful ab initio theoretical modelling successfully capturing the linear rheological response (Das et al. 2006). DOW150R is a low-density polyethylene which has been the subject of previous processing investigations (Martyn et al. 2000). All three materials were characterised in both simple shear and uniaxial extension at the same temperature as the subsequent processing experiments. Shear flow experiments were conducted with an ARES rheometer (Advanced Rheometric Expansion System, Rheometric Scientific) to obtain the linear rheological and non-linear shear flow behaviour as well the corresponding spectra. The non-linear elongational flow behaviour was characterised using the uniaxial stretching device SER (Sentmanat Elongational Rheometer, Xpansion Instruments) attached to the ARES rheometer. Specimen dimensions at test temperature were corrected to consider thermal expansion by using the room-temperature density and standard values of the thermal expansion coefficient for polyethylene. All of the rheological experiments were carried out under nitrogen atmosphere, and further rheological tests to assess the thermal stability of the

Table 1 Material properties of the three polyethylenes

Description	M_w (kg/mol)	M_n (kg/mol)	M_w/M_n	M_w (kg/mol)	η_0 (kPa s)	ρ (g/cm ³)	
						Room temp	Test temp
Linear CM1	104	50.2	2.07	104	7.9 (175 °C)	0.92	0.777 (175 °C)
HDPE HDB2	84	46	1.98	84	26.5 (155 °C)	0.958	0.78 (155 °C)
LDPE DOW150R	105	18.4	11	242	368 (160 °C)	0.921	0.782 (160 °C)

The values for HDB2 and DOW LD150R have been taken from previous work (Das et al. 2006 and den Doelder et al. 2005, respectively). It should be noted that the data in Table 1 for DOW150R (den Doelder et al. 2005) was acquired using both gel permeation chromatography (GPC) and light scattering techniques. This gives a more accurate result for branched materials than conventional GPC and leads to the different values used here than ($M_w \sim 107,000$, $M_w/M_n \sim 5.8$) quoted elsewhere (Martyn et al. 2000).

samples were conducted to ensure that the molar mass distribution and the molecular structure did not change during the experiments.

The materials exhibited increasing levels of viscoelasticity as a result of a combination of increased branching, molecular weight and temperature. The results were used to fit a set of multimode POM-POM parameters to each material, which are given in Table 2. Figure 1 shows the good visual agreement between the transient shear and uniaxial elongational viscosities and those predicted by these parameters. The contribution of each mode to the zero shear viscosity for all three materials is given in Fig. 2. This illustrates the increasing contribution of the longer relaxation modes to the zero shear viscosity, and hence viscoelasticity, from CM1 to HDB2 and finally DOW150R. A viscosity average relaxation time of the polymer, $\bar{\lambda}$, was defined as

$$\bar{\lambda} = \frac{\sum_{i=1}^N g_i \lambda_i^2}{\sum_{i=1}^N g_i \lambda_i} \quad (1)$$

where g_i is the modulus and λ_i is the relaxation time of the i th mode. The values for the three materials are given in Table 3 and further illustrate the increasing viscoelasticity for this set of polyethylenes.

The thermal stability of the materials was analysed to ensure that no significant changes of the material parameters and properties occurred during the subsequent processing experiments. Dynamic-mechanical time sweeps in the linear viscoelastic region (at sufficiently low angular frequencies near the Newtonian flow regime) were used as a sensitive indicator for this purpose. Results for the three materials at the test temperatures are shown in Fig. 3 where the elastic modulus of each sample is plotted versus

time. The upper and lower limit at which the modulus has changed by 5% is indicated by the solid line and is used as the stability criterion, and the angular frequencies were chosen individually to account for the longest relaxations time of the different materials. From the plot, it can be seen that a sufficient thermal stability is granted for the materials and temperatures used in the subsequent processing experiments for at least 10^4 s.

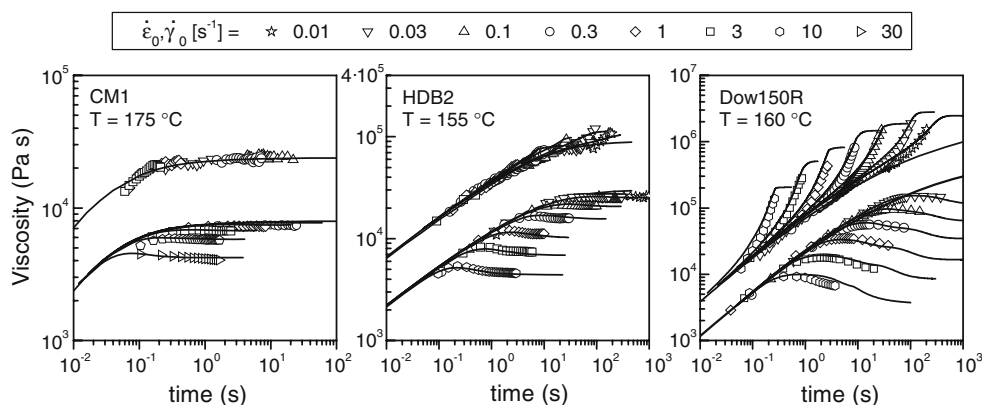
The stress optical coefficient (SOC) at the processing temperature for each material was calculated using a technique similar to that reported previously (Lodge 1955) which relates the pressure drop across a long slit to the slit wall fringe order, and further details can be found elsewhere (Coventry 2006). The values and their corresponding values of PSD per fringe for this work are given in Table 4. To verify this technique, comparisons were made to another technique (Clemeur et al. 2004a), which evaluates the SOC by interpolating the central fringe order progression within a long slit to the wall. Values obtained with these two techniques were found to be in quantitative agreement with one another and gave values within the literature range for polyethylene of $1.2\text{--}2.4 \times 10^{-9} \text{ Pa}^{-1}$ (Macosko 1994). It should be noted that the possible error of these results, due to the fringe counting technique employed at low fringe order regions, can be of the order of 25%. This is an important consideration when comparing experimental results to computational simulations. It was noted that the SOC calculated in this work for the low-density polyethylene (LDPE) is substantially different from the value of $3.53 \times 10^{-9} \text{ Pa}^{-1}$ reported previously (Martyn et al. 2000). No obvious explanation can be made for this discrepancy, as the techniques used were similar. As $3.53 \times 10^{-9} \text{ Pa}^{-1}$ is outside the literature range for polyethylenes, the value obtained in this work is used in subsequent comparisons of experimental and computational work.

Table 2 POM-POM parameters used in the equations outlined in “Numerical simulations” fitted to linear and uniaxial extensional data using techniques similar to those presented in Inkson et al. (1999)

Linear (CM1) at 175 °C				HDPE (HDB2) at 155 °C				LDPE (150R) at 160 °C			
λ_i	g_i	q_i	r_i	λ_i	g_i	q_i	r_i	λ_i	g_i	q_i	r_i
0.001	239,915	1	1	0.002757	440,450	1	1	0.0316	49,451.13	1	1
0.00316	124,746.3	1	1	0.014399	84,470	1	1	0.1	21,039.7	1	1
0.01001	130,951.9	1	1	0.075211	30,174	1	1	0.3163	13,849.04	2	1
0.03166	78,308	1	1	0.39286	9,450.4	1	1	1	9,626.96	18	4
0.10016	18,257.67	1	1	2.0521	3,802.1	1	1	3.1623	6,070.23	20	4
0.31685	2,119.34	1	1	10.719	729.26	2	1	10	3,519.47	20	4
1.00236	325.27	1	1	55.999	64.8	4	2	31.6228	1,783.64	20	3
3.17099	50.95	1	1	292.46	3.58	5	3	100	797.38	25	4
10.03148	10.423	1	1	–	–	–	–	316.228	288.16	40	2
31.73478	0.06715	2	1	–	–	–	–	1,000	74.004	55	3
–	–	–	–	–	–	–	–	3,162.28	13.69	20	3

The software used was *Reptate*, developed as part of the microscale polymer processing 2 project by Jorge Ramirez and Alexei Likhtman.

Fig. 1 Transient shear and transient uniaxial elongational viscosity of CM1, HDB2 and DOW150R at different strain-rates between 30 and 0.01 s⁻¹. The lines are model calculations using the POM-POM model parameters (cf. Table 2)



Processing experiments

A Cambridge MPR (Mackley et al. 1995) was used for the processing experiments and its application with an optical configuration has been previously described by a number of authors (see for instance Collis and Mackley 2005). The MPR is a dual piston capillary-type rheometer designed for small quantities of material (~10g of polymer) and consists of three sections. The top and bottom sections contain reservoirs for the polymer material, servo hydraulically driven pistons and pressure/temperature transducers. The midsection enables simultaneous pressure and optical measurements to be made and resembles a cube with holes in all six faces. The vertical faces accept a pair of stainless steel die inserts in one direction and a pair of 15-mm depth stress-free quartz windows in the other, whilst polymer flows through the top and bottom holes. All three sections are surrounded by heating channels and insulation. Whilst the heating jackets ensure a constant temperature around the three sections, heat losses are likely to occur through the quartz windows, although these are expected to be small.

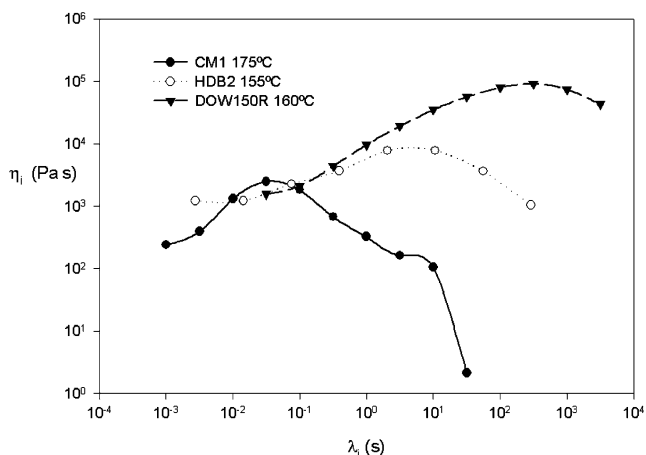


Fig. 2 Plot of zero shear viscosity of each relaxation mode, $\eta_i = G_i \times \lambda_i$, as a function of relaxation time, λ , using the multi-mode POM-POM model parameters of CM1, HDB2 and DOW150R as indicated in Table 2

Two different geometries were investigated. The first was a CE slit geometry similar to those used in previous work (see for instance Collis and Mackley 2005). This geometry creates regions of high simple shear near to the slit walls and extensional flow in the region of the symmetry line in the inlet and outlet areas of the flow. The second is a cross-slot geometry. This flow configuration creates a pure shear flow deformation in the central region about the stagnation point of the flow, together with essentially simple shear near the outer curved walls (see for instance Coventry and Mackley 2008).

The two insert geometries used during this study are shown in Fig. 4. For the CE slit inserts, the material can be repeatedly passed through the midsection, from one reservoir to the other and back again at different flow rates, allowing multiple experiments to be performed on one sample. Optical observation of the CE slit section enabled interrogation of the entry and exit flow together with flow within the slit. The inserts used for the cross-slot geometry utilised slave pistons which used a pressurised nitrogen system to facilitate multi-pass operation. The system was developed by Coventry (2006) and is reported by Coventry and Mackley (2008). During operation, the two MPR pistons are moved towards one another at a controlled rate, pushing material through the top and bottom of the insert and out through two horizontal side channels. Slave pistons in these horizontal channels maintain the material within the MPR, and the subsequent retraction of the pistons to their original position allows the pressurised nitrogen to force the material back through the cross-slot and into the top and bottom reservoirs.

Table 3 Mean relaxation time (as defined by 1) for the three materials

Material	Linear (CM1) at 175 °C	HDPE (HDB2) at 155 °C	LDPE (DOW150R) at 160 °C
$\bar{\lambda}$	0.325	21.28	1,127

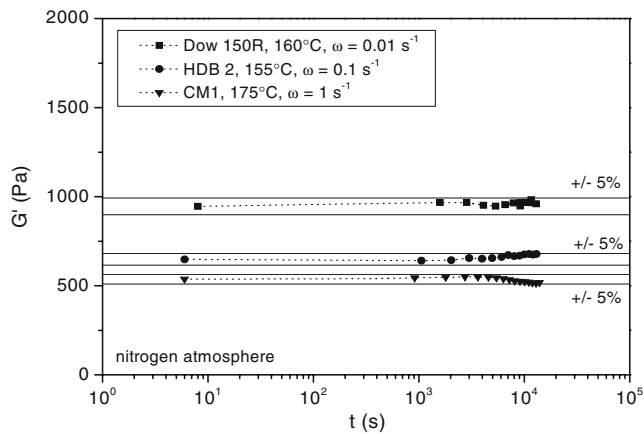


Fig. 3 Dynamic-mechanical time sweeps for CM1, HDB2 and DOW150R at different temperatures under nitrogen atmosphere showing a thermal stability of at least 10⁴ s

Both geometries have been used in previous work (Coventry and Mackley 2008; Hassell and Mackley 2008) and are 10-mm-deep. Whilst the cross-slot and contraction–expansion slit have aspect ratios of around 7, equating approximately to two-dimensional flow (Wales 1976), the inlet and outlet to the contraction expansion have an aspect ratio of order 1, and thus, three-dimensional flow is expected in this region. Previous work has concluded that this three-dimensional effect may not have a great impact on the observed birefringence (Clemeur et al. 2004b). However, more recent studies of linear LDPE and LDPE in a contraction geometry (Hertel et al. 2007) have shown that the flow field into the slit is increasingly three-dimensional with increasing branching. Three-dimensional flow effects are expected within the entrance region of the slit for the more branched materials. In all cases, the assumption of two-dimensional flow is only approximate, and the results reported here are expected to deviate quantitatively slightly from the ideal two-dimensional case.

Stress-induced birefringence was used to observe the PSD during flow. Monochromatic polarised light with a wavelength of 514 nm was passed through the midsection and orthogonal analyser before being captured using a digital video camera. Quarter wave plates were used to eliminate the isoclinic extinction bands and leave only the stress-related isochromatic fringes.

Table 4 Experimentally obtained SOC for the materials and corresponding PSD value per fringe for the experiments

	CM1 at 175 °C	HDB2 at 155 °C	DOW150R at 160 °C
SOC × 10 ⁹ (Pa ⁻¹)	1.29	2.34	2.10
Stress per fringe (Pa)	40,000	22,000	24,500

The flow through the two geometries was characterised in the following way. The apparent wall shear rate used to characterise flow through the CE slit was based on the solution for Newtonian flow through infinite parallel plates and is given by,

$$\dot{\gamma}_{app} = \frac{6Q}{w^2l} = \frac{6r_p^2\pi V_p}{w^2l} \tag{2}$$

where Q is the volumetric flow rate (mm³ s⁻¹), w is the width of the slit (1.4 mm), l is the depth of the slit (10 mm), r_p is the piston radius, and V_p is the speed of the pistons (mm s⁻¹).

The central extension rate in the cross-slot was estimated from the flow geometry, and the relationship between the maximum extension rate and the piston speed was defined as,

$$\dot{\epsilon}_{max} = AV_p \tag{3}$$

where A is a constant defined by the geometry. As an approximation, the centre line velocity accelerates from zero at the centre to the maximum channel velocity within the cross-slot over a distance equal to the channel width. Numerical simulations using a Newtonian and integral Wagner model were initially performed by Coventry (2006) and found A to be equal to approximately 8, which is higher than the value of 7 V_p calculated using the definition outlined by others (Peters et al. 1999, Soulages et al. 2007). Subsequent modelling using the multimode POM-POM constitutive model for various lightly branched polyethylenes found A equal to 8.6, and this value was used in the subsequent sections.

Numerical simulations

Numerical simulations were carried out using the Lagrangian–Eulerian time-dependant solver *flowSolve* (Harlen et al. 1995) to compute the predicted PSD for the experimental conditions. The multimode POM-POM model was used,

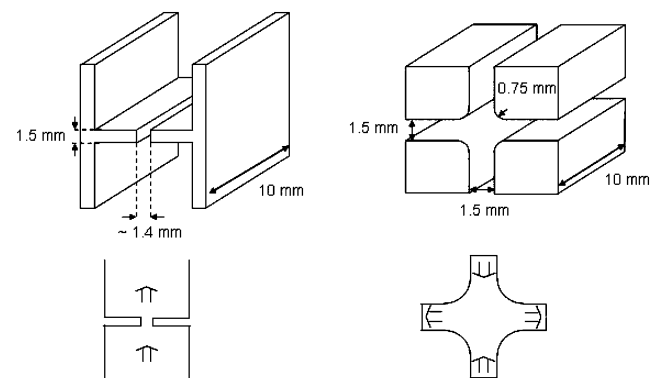


Fig. 4 The geometries used in the MPR mid-section and associated flow directions for (left) the slit and (right) the cross-slot

which is based on tube theory for a branched molecule having two q -armed stars connected by a backbone segment (McLeish and Larson 1998; Inkson et al. 1999). In the model, the polymer backbone is considered to have two different characteristic relaxation times, one for the stretch (τ_s) and the other for the orientation (τ_b) of the backbone. The ratio of these is denoted as r_i , where $r_i = \tau_b/\tau_s$. Application of this model to a randomly branched polymer mixture is equivalent to a decoupling approximation for the different levels of branching in the constituent molecules (Inkson et al. 1999). The central equation for stress is given in terms of backbone stretch, $\lambda(t)$, and the orientation tensor, $\mathbf{S}(t)$. A subsequent refinement to the model was the consideration of drag–strain coupling between relaxed and stressed chain segments, which adds an exponential term to the stretch equation (Blackwell et al. 2000). Once the stress is calculated, it is coupled with the force and mass conservation equations to model the flow at each time step. The multimode POM-POM model used for the numerical simulations carried out in this paper are given by:

$$\boldsymbol{\sigma}(t) = \sum_i \boldsymbol{\sigma}_i = 3 \sum_i g_i \lambda_i^2(t) \mathbf{S}_i(t) \quad (4)$$

$$\mathbf{S}_i(t) = \frac{\mathbf{A}_i(t)}{\text{tr} \mathbf{A}_i(t)}, \frac{D\mathbf{A}_i(t)}{Dt} = \boldsymbol{\kappa} \cdot \mathbf{A}_i + \mathbf{A}_i \cdot \boldsymbol{\kappa}^T - \frac{1}{\tau_{bi}} (\mathbf{A}_i - \mathbf{I}), \quad (5)$$

$$\frac{D\lambda_i(t)}{Dt} = \lambda_i(t) \boldsymbol{\kappa} : \mathbf{S}_i - \frac{1}{\tau_{si}} (\lambda_i(t) - 1) \exp\{\nu_i^* (\lambda_i(t) - 1)\}, \quad \lambda_i \leq q \quad (6)$$

The Lagrangian implementation of this model uses a triangular mesh, which is transported with the flow for each time step of the simulation. At time zero, only the boundaries are specified, and the program fills the area with a regular distribution of vertices at a specified density. The stresses across this grid are then calculated from the constitutive parameters and boundary conditions, and a solution is found for the velocities and pressures at each vertex. The triangular elements deform according to these velocities, and the constitutive parameters, which are associated with the elements rather than vertices, update to reflect the deformations. The grid is checked to split triangular elements that have become too large, reconnect those which have been highly deformed to control their maximum aspect ratio, delete those which have become too small and add new elements at inflow boundaries before moving to the next step. For both geometries, a symmetry plane was used to reduce computational time, no-slip boundary conditions were used at the walls, and the inlet was modelled based on

a steady state one-dimensional solution to shear flow (Lee et al. 2001). Simulations were performed on a 1.7-GHz Intel laptop and took between 12 and 48 h to run depending on mesh refinement and geometry.

Results and discussion

Experimental observation

The basic experimental flow birefringence behaviour of the three chosen polymers in both the CE slit and cross-slot is shown in Fig. 5. Different processing temperatures were chosen to highlight more clearly the effects of increasing viscoelasticity. The apparent wall shear rate for the CE slit flow was $\sim 12 \text{ s}^{-1}$, and for the cross-slot flow, the central extension rate was $\sim 1.9 \text{ s}^{-1}$ with a wall shear rate of $\sim 4.9 \text{ s}^{-1}$. For CM1, which has the lowest level of viscoelasticity, the PSD pattern shows the classic behaviour of a near-Newtonian response for the two geometries (see for instance Coventry 2006) seen in Fig. 5a and d. The pattern is symmetric between the inlet and outlet in both cases and illustrates that the materials' current level of stress is not sensitive to its deformation history. As the viscoelasticity of the material within the flow increases, the material becomes increasingly sensitive to past deformations, and the PSD profile becomes increasingly asymmetric. This is shown for HDB2 in Fig. 5b and e where an increasing asymmetry is observed for both geometries. In the case of the CE slit, an increasing asymmetry between the inlet and outlet symmetry plane is observed, and the "zero stress eye", shown as an arrow in Fig. 5a–c, moves away from the centre of the CE slit. For the cross-slot, the level of asymmetry between the inlet and outlet increases, and cusping of the fringes along the outlet centre line is observed, in a similar way to previous observations (Verbeeten 2001; Coventry and Mackley 2008). For the most viscoelastic material, DOW150R, shown in Fig. 5c and f, a number of interesting features are found. For the CE slit, the formation of stress fangs is observed similar to that previously reported (Lee et al. 2001), whilst the upstream vortices near the wall and entrance to the CE slit have an increased effect upon the stress. For the cross-slot, highly localised central fringes are observed close to the stagnation point, and the formation of "W cusps" occurs along the outlet centre line. The formation of this "W cusp" has been observed for other highly branched materials using both the MPR (Hassell and Mackley 2008) and elsewhere (Soulages et al. 2007), and this will be discussed in more detail in subsequent work. It is thought to be the result of extreme strain hardening at the centre line, and the appearance of this local singularity may be related to "birefringent pipes" reported for exit flow in certain polymer solutions (Harlen et al. 1990, 1992).

Also seen for the cross-slot geometry at higher material viscoelasticity and flow rates are extensional inlet effects, which encroach into the cross-slot region from the upstream entrance. This is seen in the cases of HDB2 and DOW150R shown in Fig. 5e and f and is represented as a white fringe at the inflow centre line. It indicates a greater than zero PSD, and the entrance flow in these instances is not a fully developed shear flow. This is a result of the geometry of the inserts (see Coventry and Mackley 2008), with a contraction located upstream of the cross-slot. This will affect any comparison between simulations and experimental work and is discussed in the subsequent section.

An important issue with the high extensional flow within the cross-slot is the validity of the stress optical rule (SOR). Recent work for polystyrene melts (Venerus et al. 1999) found a deviation of the stress optic rule above roughly 1 MPa in uniaxial extension flow, and this value has been

found to increase with decreasing polydispersity and increasing Weissenberg number (Luap et al. 2006). No similar work has been found for either planar extension or polyethylene melts, but the maximum values of the PSD presented here, based on the stress optical coefficients in Table 4, were ~ 0.11 MPa (CM1), ~ 0.16 MPa (HDB2) and ~ 0.35 MPa (DOW150R). In all cases, these values are well below the 1 MPa limit, and thus, from the information available in the literature at this time, the SOR is assumed to be valid for all the experiments considered.

For both geometries, and for the flow conditions used, it is important to ascertain whether a steady-state stress profile is obtained for each of the three materials. For the 20-s duration of each experiment, both for the CE slit and cross-slot, it was clear for CM1 and HDB2 (Fig. 5a,b,d and e) that a steady-state stress pattern was observed within 2 to 5 s of flow start-up. For DOW150R in the CE slit, whilst most of the stress field appeared to equilibrate within 10 s, the downstream stress fang pattern was still evolving up to the cessation of flow. In the case of the same polymer in the cross-slot (Fig. 5f), an apparent steady state was observed to have been reached before the end of the experimental duration.

In both geometries, material flows along different streamlines, and therefore the residence time within the optical region, is a function of the materials initial position. In the CE slit, the material which has been previously subject to high strain rates close to the slit wall, and is therefore highly stressed, is subsequently convected downstream into a region of low strain rate and high residence time. Consequently, the long relaxation times of DOW150R result in the experimental observation of slow stress relaxation in these regions, which continues to affect the stress pattern up to the cessation of flow. For the case of the cross-slot, the residence time for material is proportional to the proximity of its streamline to the inlet/outlet centre line and the stagnation point (see for instance Crowley et al. 1976). Material along the inlet/outlet symmetry plane (highlighted in Fig. 6b as the dotted line) experience long residence times within the region of highest extension. The highest PSD is observed here, and unlike in the CE slit, this highly stressed material then travels to a region of low residence time along the outlet centre line. The subsequent long time stress relaxation in the cross-slot is therefore not observed within the field of view.

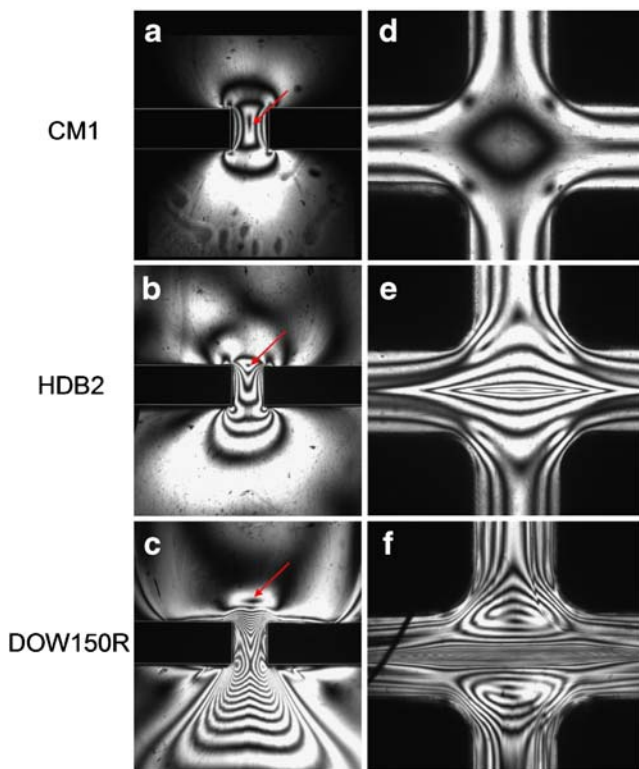


Fig. 5 Flow-induced birefringence images for the three materials within **a–c** the CE slit at a flow rate of $\sim 39.3 \text{ mm}^3 \text{ s}^{-1}$, apparent wall shear rate of $\sim 12 \text{ s}^{-1}$ and **d–f** the cross-slot at a flow rate of $\sim 34.56 \text{ mm}^3 \text{ s}^{-1}$ per inlet, maximum central extension rate of $\sim 1.9 \text{ s}^{-1}$. Materials are **a** and **d** CM1 at 175°C , **b** and **e** HDB2 at 155°C and **c** and **f** DOW150R at 160°C . The *red arrows* in **a–c** highlight the “zero stress eye”. The *black line* in the left exit channel of **f** was a piece of material outside the geometry which separated from an O-ring during the experiment and could not be removed without affecting the optical setup. Direction of the flow (illustrated in Fig. 4) is vertically upwards for the CE slit. Materials flow into the cross-slot through the vertical channels and out through the horizontal ones. As a representation of scale, the CE slit length and cross-slot channel width are both 1.5 mm

Comparison with simulation

The match between experimental and simulation results for HDB2 is presented in Fig. 6 for (a) the CE slit and (b) cross-slot geometries. The apparent wall shear rate for the CE slit flow was $\sim 12 \text{ s}^{-1}$, and for the cross-slot flow, the central extension rate was $\sim 1.9 \text{ s}^{-1}$, with a wall shear rate of $\sim 4.9 \text{ s}^{-1}$. For the CE slit, the match between the experiment and simulation is good, with the simulation accurately

capturing both the stress profile and the number of fringes. Two slight discrepancies are observed downstream of the slit exit. The first is the observation of a slight fang structure observed at the outlet of the simulation which is not seen in the experiment. Whilst uncertain, it is possible that this is a two-dimensional effect that is not fully captured by the experiment due to the three-dimensional nature of the inlet and outlet regions of the CE slit. The second is the observation in the experiment (Figs. 5b and 6a) of a fringe at the upstream and downstream corners of the flow. In the case of this experiment, this is the result of residual stress within the quartz windows and could lead to a slight discrepancy (plus 0.25 to 0.5 of a fringe) for the comparison between experiments and simulation.

For the cross-slot geometry, the experimental inlet flow is not a fully developed shear flow as a result of the upstream extensional effects mentioned previously. This extension is at 90° to the extension subsequently produced along the cross-slot centre line and produces a PSD due to light retardation in the materials principle axes at 90° to that resultant from the cross-slot. After the inlet, the extensional flow in the cross-slot re-orientates and stretches the material such that the PSD moves back through zero due to the change in the principal axis of the light retardation. This is similar to the effect which causes the “zero stress eye” at the outlet of the CE slit and cannot be taken into account in the computation, as the simulated results prescribe a fully developed solution on the inlet boundary. If the model is accurate, this will lead to an over-prediction of the PSD in the simulation compared to that experimentally observed due to the initial PSD present within the material entering the cross-slot. The simulation shown in Fig. 6b accurately predicts both the general shape of the PSD and the cusping along the inlet–outlet centre line. However, the quantitative comparison is less accurate, and the simulation under-predicts the PSD. This disagreement is worse when these experimental inlet effects are taken into account and indicates that the model is failing to capture some of the effects of this strongly extensional flow and high strain close to the stagnation point. Although the reason for this is unclear, one possible explanation is that the behaviour of the material in moderate extension rates with long residence times, which is not probed by the CE slit flow, was not accurately captured in the uniaxial rheology experiments. This is possible, as the samples can break before Hencky strains higher than 3 are reached.

A quantitative comparison of the stress along the axis of symmetry for the CE slit (the dashed line in Fig. 6a) for all three materials is given in Fig. 7. This gives an indication of the performance of the computational predictions over a range of apparent wall shear rates ($4.2\text{--}24\text{ s}^{-1}$) for the three materials and is a technique used successfully in previously work (see for instance Park et al. 1992; Kiriakidis et al.

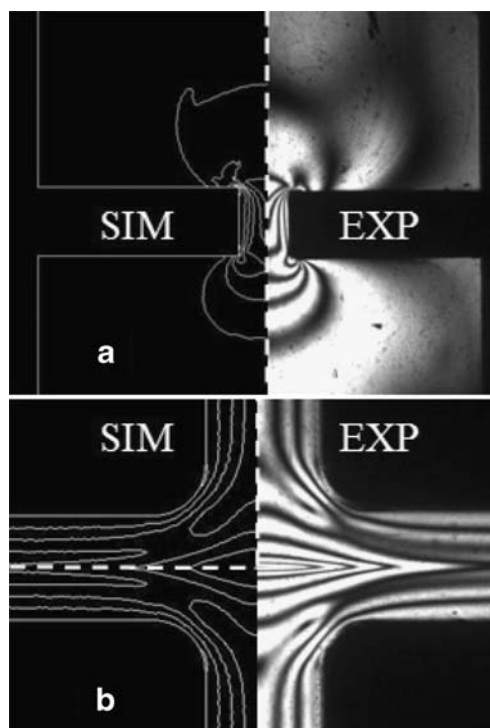


Fig. 6 Comparison between experimental and computational principal stress difference results for HDB2 at 155 °C within **a** the contraction–expansion slit at flow rate of $\sim 39.3\text{ mm}^3\text{ s}^{-1}$, apparent wall shear rate of $\sim 12\text{ s}^{-1}$ and **b** the cross-slot at a flow rate of $\sim 34.56\text{ mm}^3\text{ s}^{-1}$ per inlet, maximum central extension rate of $\sim 1.9\text{ s}^{-1}$. Direction of the flow (illustrated in Fig. 4) is vertically upwards for the CE slit. Materials flow into the cross-slot through the vertical channels and out through the horizontal ones. As a representation of scale, the CE slit length and cross-slot channel width are both 1.5 mm

1993; Bent et al. 2003). For the most Newtonian-like behaviour, shown by CM1, the agreement between the experiment and simulation is excellent. The model accurately captures the development and relaxation of the PSD as the polymer flows into and out of the CE slit. Of the three materials used, this is the most accurately rheologically characterised due to its relatively narrow relaxation spectrum distribution, including the contribution to the Maxwell modes by the high molecular weight (HMW) chains. It is therefore expected that this gives the best agreement between experiments and simulations. The similar comparison for HDB2 shows that the simulations slightly over-predict the PSD at the lowest rate and slightly under-predicts the PSD at the highest two rates. If the residual stress observed in this experiment from the window (equating to a worst case scenario of a discrepancy of half a fringe) is taken into account, then the simulation for the two highest rates would match the stress levels at the inlet to the slit. For all three flow rates, the PSD at the outlet of the slit is over-predicted, with an increasing discrepancy with increasing flow rate. This could be the result of the three-dimensional nature of the flow in the experiment or the simulation not accurately capturing the velocity field exiting

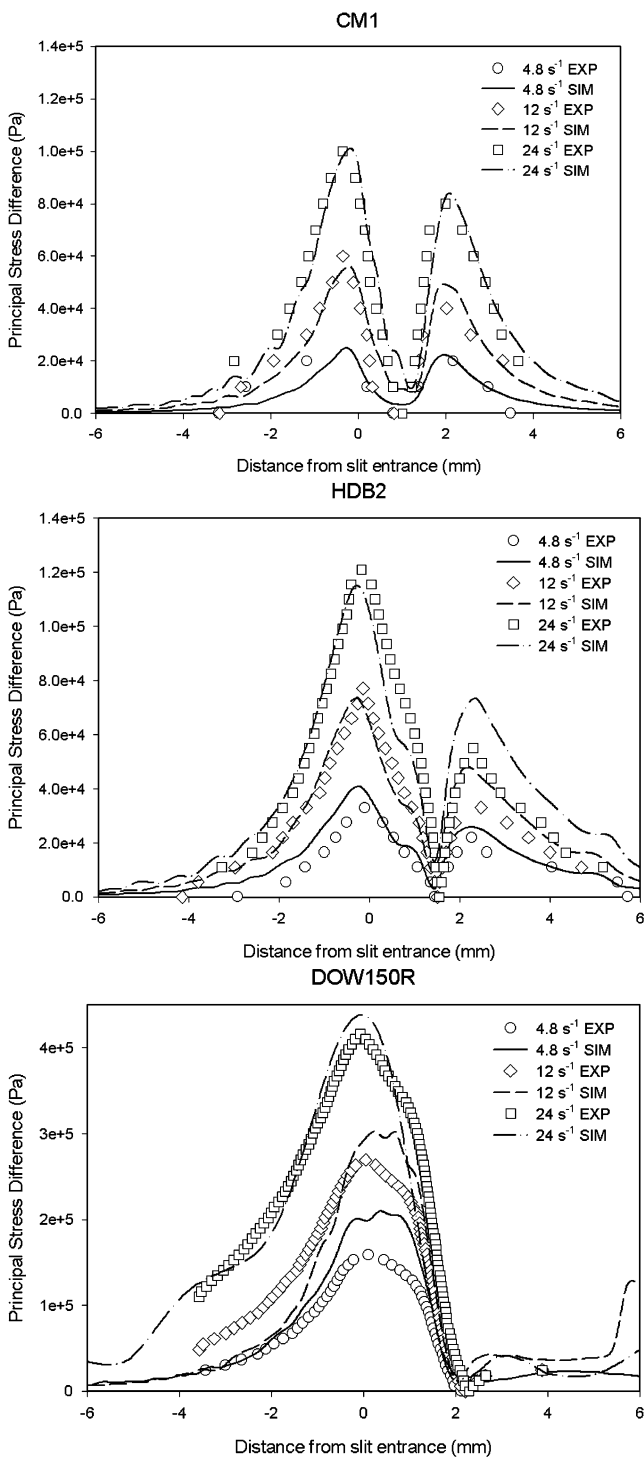


Fig. 7 Principal stress difference profile comparisons between experiments (*points*) and simulations (*lines*) along the contraction–expansion slit centre line (outlined in Fig. 6a) for CM1 (*top*), HDB2 (*middle*) and DOW150R (*bottom*)

the CE slit and the associated downstream vortices. Although further work would be required to identify the reason for the difference, the general agreement is good and easily within the error both in the prediction of the SOC and that found for wall effects (Schoonen 1998).

For DOW150R, the most viscoelastic material, the simulation slightly over-predicts the stress at the lower two flow rates but accurately captures the stress at the highest rate. Again, the shape of the stress development along the centre line and its subsequent relaxation downstream of the slit is well captured. It should be noted that due to computational limitations, the simulations were run for lower times than the experiments (and hence a higher De). This results in the downstream peak observed for the higher two rates, which is the result of the fang having not fully developed downstream to the wall and its effects being seen along the symmetry centre line.

The greater entrance effects due to both shear stresses at the window and quicker PSD relaxation after the entrance to the slit, both observed for three-dimensional flows (Clemeur et al. 2004a) were not noticeable in this work. This increasing three-dimensional effect was found with increasing flow rate, which could explain the transition from over- to under-prediction of PSD with increasing flow rate for CM1 and HDB2 and the opposite effect for DOW150R. Hence, the effect of branching on the three-dimensionality of the experiment is another possible reason for the observed discrepancies, having previously been found to effect the flow field for LDPE entering a CE slit (Hertel et al. 2007).

A comparison of the pressure drops for simulated and experiment results for all materials and shear rates within the CE slit is given in Fig. 8, and the relative error in pressure predictions are shown in Table 5. Although the PSD is well captured for the three materials, the pressure drop across the system is consistently below that found in experiments. The general trend is for an increasing under-prediction of the pressure drop with increasing viscoelasticity. Whilst for CM1 and DOW150R the percentage under prediction is similar for all three flow rates, this is not the case for HDB2, with the reason for this being unclear.

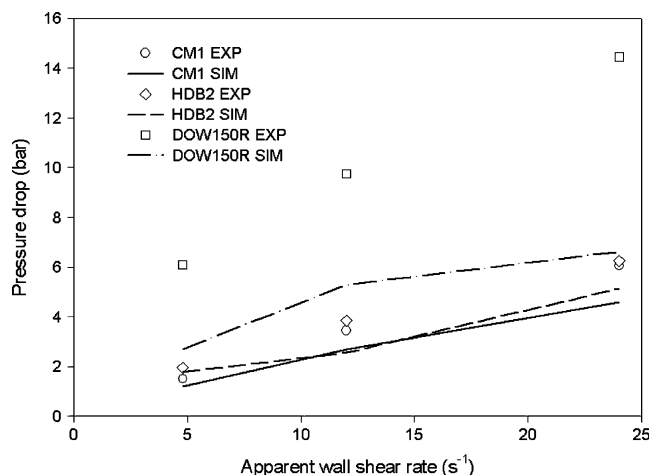


Fig. 8 Pressure difference comparisons between experiments (*points*) and simulations (*lines*) for all three materials

Table 5 Relative error in pressure prediction (in %) between experiment and simulations for the contraction–expansion slit geometry

$\dot{\gamma}_{app}$ (s^{-1})	CM1	HDB2	DOW150R
4.8	19.3	8.9	56
12	22.3	33.6	46
24	24.1	17.9	54

Difference is defined as $[(P_{exp} - P_{sim})/P_{exp}] \times 100$.

Previous studies have shown similar differences in entrance correction factors for LDPE materials in circular (Barakos and Mitsoulis 1995) and slit dies (Mitsoulis et al. 2003) using an integral K-BKZ model. Here, the level of strain hardening in a material and the Hencky strain present at the inlet was highlighted as a possible reason for the pressure drop discrepancies. Whilst there is an increasing error in this work between simulation and experimental pressure drop results with increasing strain hardening, it does not explain the good agreement with PSD. This mismatch is an important observation, as the pressure drop should be linked to the observed stresses, with any successful prediction of PSD corresponding to an equivalent match in pressure drop.

A similar quantitative comparison to that presented in Fig. 7 for the CE slit is shown for the cross-slot in Fig. 9. This compares the stress along the inlet–outlet centre line of the flow (the dashed line in Fig. 6b) for CM1 and HDB2. As before, the comparison is made over a range of maximum extension rates (~ 0.76 – $3.8 s^{-1}$) and wall shear rates (~ 1.84 – $9.2 s^{-1}$). For the least viscoelastic material, CM1, the match between experiment and simulation at the lower two extension rates is again good, whilst at the higher extension rate ($3.8 s^{-1}$), the simulation over-predicts the PSD profile. In all three cases, the simulations qualitatively capture the increase in PSD asymmetry associated with the higher rates of deformation and the match along the inlet–outlet centre line is good.

In the case of HDB2, the match at the lowest extension rate is good, whilst at the higher rates, unlike for CM1, the simulation under-predicts the PSD. For these higher rates, the relaxation decay at the outlet is quantitatively captured, but the high rate of increase in the PSD at the inlet is not. The experimental inlet effects are observed for these higher rates and the PSD along the centre line starts positive rather than at zero. Given this observation, the under prediction by the simulations of the PSD at these higher rates is even more pronounced and could be a result of the failure of the rheology to capture the longer relaxation modes. This can be visualised in Fig. 2 as a continuation of the HDB2 curve to higher relaxation times where this additional contribution would be caused by the HMW chains. In the high

extensional regions close to the stagnation region within the cross-slot flow, these chains will be subjected to higher strain (Crowley et al. 1976) and thus affect the PSD pattern observed in the experiments. It was not possible to run simulations for DOW150R, as they would not reach convergence. One possible reason for this could be the requirement for unfeasibly fine meshes to be employed near the stagnation region of the cross-slot, given the effect of mesh refinement found in areas of high stress gradients in the CE slit flow.

In the case of all three materials, the simulations give good predictions of the PSD profiles over a range of flow conditions in the CE slit, accurately capturing the material behaviour in regions of high shear. However, the model using the same rheological parameters fails to accurately capture PSD patterns for similar materials in cross-slot flow where regions of high strain, residence time and extensional rates are present. There are three possible explanations for these observations: (1) The POM-POM model does not accurately capture the molecular behaviour in these highly orientating flows; (2) its implementation in *flowSolve* results in discrepancies in its ability to model these highly orientating flows; and (3) the rheological characterisation has failed to accurately capture the longer relaxation modes within the material, associated with the HMW chains which have a greater affect in the high strain flow. If it is a result of the rheological characterisation, it is unclear why this would lead to an over-prediction of the PSD for CM1 at the highest extensional rate. However, it would explain why, for the lowest rate, the HDB2 PSD profile is accurately captured, whilst at higher rates where higher molecular orientation is found, and thus the HMW chains have a greater influence, the simulations under-predicts the PSD.

Time dependence of stress profile

So far, the PSD development has been characterised for increasing levels of viscoelasticity in the two flows outlined by varying the flow rates (analogous to varying the Weissenberg number, We). A similar pattern can be observed in these two flows by varying time as a parameter (analogous to varying the Deborah number, De) for a constant flow rate (We). Figure 10 shows the PSD development for DOW150R in the CE slit flow at an apparent wall shear rate of $\sim 12 s^{-1}$, as a function of time, and illustrates elegantly the development of the PSD pattern. At low De , the material has a Newtonian profile similar to that observed in Fig. 5a for CM1 due to the absence of any past stress–strain history and hence viscoelastic effects. As time develops and the material is subjected to further deformation, whereby the materials memory can influence the stress pattern, the PSD profile develops an increasing asymmetry. These transient profiles

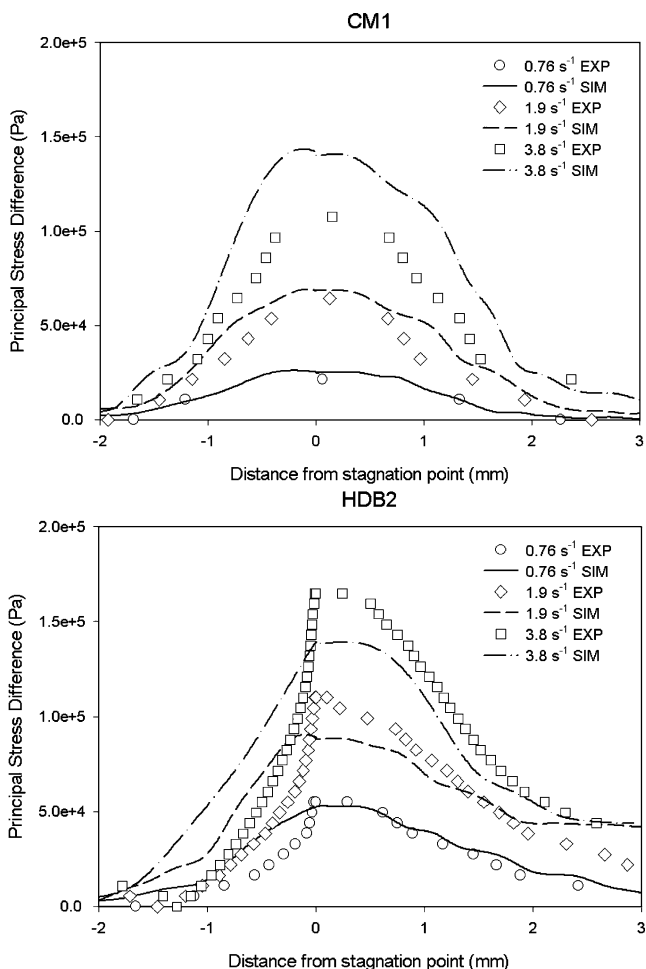


Fig. 9 Principal stress difference profile comparisons between experiments (*points*) and simulations (*lines*) along the cross-slot inlet outlet centre line (outlined in Fig. 5b) for CM1 (*top*) and HDB2 (*bottom*)

also capture the development of the stress fangs observed previously (Lee et al. 2001) from the outlet corners of the slit and their propagation downstream. As can be seen from Fig. 10b–f, this development is complex, with very high PSD gradients, represented by closely packed fringes, around the area of the fangs and close to the slit wall. This localisation of the PSD fringes makes accurate comparison with simulations for this particular material and flow rate difficult and is illustrated in the corresponding simulation results given in Fig. 11. Here, the transient development of the PSD pattern is captured at times corresponding to Fig. 10a–e and illustrates the predicted development of the stress fangs. The PSD gradients are highest at the wall and at positions downstream where these high gradient regions are advected downstream over time. This is similar to the previous experimental observations in Fig. 10. The simulation also captures the upstream PSD development from an initial “C shape” (Figs. 10b–e and 11a–d) similar to those observed for the other two materials (Fig. 5a and b) to a “butterfly wing” shape (Figs. 10f and 11e). Whilst in

general the simulation captures well these transient features, it over-predicts the time required for the development of the stress fangs and under-predicts the time required for the development of the “butterfly wings”. It is possible that both these failings could be accounted for by the three-dimensional nature of the flow up and downstream of the slit. Subsequent rounding of the slit corners will reduce these localised gradients and may allow better comparison between experiments and simulations.

Figure 12 shows a similar time evolution for HDB2 in the cross-slot geometry for a central extension rate of $\sim 7.6 \text{ s}^{-1}$ and a wall shear rate of $\sim 19.6 \text{ s}^{-1}$ using both experimental (Fig. 12a–c) and computational (Fig. 12d–e) techniques. Again, at low De , the material has a Newtonian profile similar to that observed in Fig. 5d for CM1. As in Fig. 10, as the flow evolves, the past deformation of the material enhances the effect of material memory on the PSD pattern. This results in increasing levels of asymmetry between the inlet–outlet centre line and cusping along the outlet centre line. The cusping is a result of the high extension rate and residence time experienced by the material along the centre line. Comparison between the experimental and simulation results shows that the simulation accurately captures quantitatively the development of

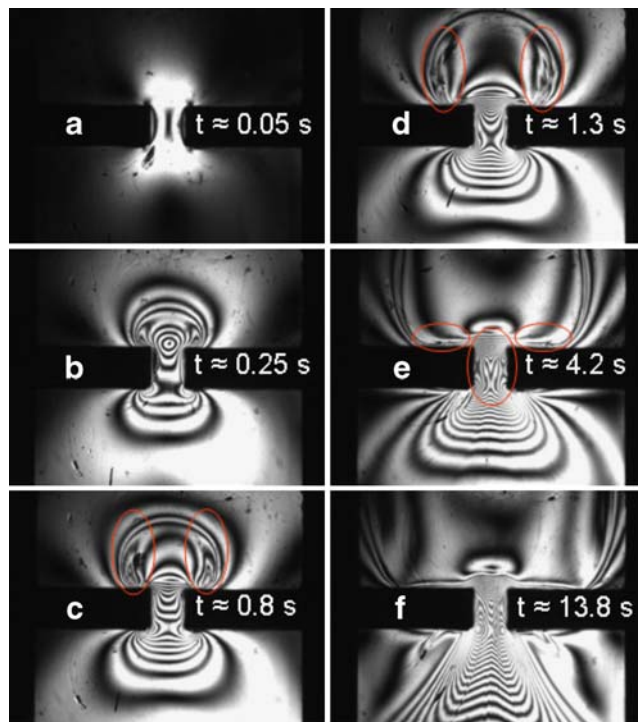


Fig. 10 Transient flow induced birefringence images for DOW150R at a flow rate of $39.3 \text{ mm}^3 \text{ s}^{-1}$, apparent wall shear rate of $\sim 12 \text{ s}^{-1}$ (a–f). The development of the stress fangs is highlighted by *circles* along with e the formation of small secondary fangs close to the slit wall and more complex slit PSD profile. Direction of the flow (illustrated in Fig. 4) is vertically upwards. As a representation of scale, the CE slit length is 1.5 mm.

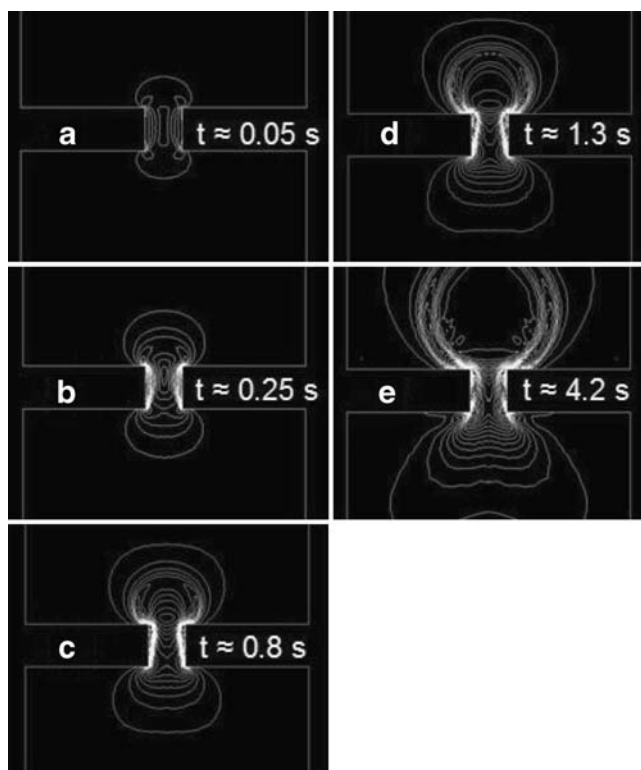


Fig. 11 Simulation results corresponding to the images shown in Fig. 10 for DOW150R in the CE slit (a–e). Direction of the flow (illustrated in Fig. 4) is vertically upwards. As a representation of scale, the CE slit length is 1.5 mm

this increasing asymmetry. However, the simulation development outlined in Fig. 12d–e under-predicts the PSD gradients observed close to the stagnation point. The reasons for this are likely to be similar to those outlined in the last paragraph of “Comparison with simulation”. Both Figs. 10 and 12 illustrate the enormous information on the materials behaviour which can be obtained by varying the time in a similar manner to varying material viscoelasticity.

Conclusions

The effect on the PSD profile of increasing levels of viscoelasticity within polyethylene was captured in two flow geometries using flow-induced birefringence. In both flows, the PSD developed from an initial Newtonian profile to increasing levels of asymmetry between the inlet and the outlet flow. In the CE slit, at high levels of viscoelasticity, the formation of upstream vortices and downstream stress fringes were observed, similar to previous work (Lee et al. 2001). In the cross-slot, increasing viscoelasticity results in cusping along the outlet centre line, whilst further increase resulted in highly localised fringes on the outlet centre line and the formation of “W” cusps similar to those observed elsewhere (Soulages et al. 2007).

Subsequent comparisons between these results and multimode POM-POM simulations performed using *flow-Solve* were then successfully performed for all cases but the most highly viscoelastic material in the cross-slot flow. For the CE slit, the simulations accurately captured both qualitatively and quantitatively the development of the PSD pattern for the CE slit flow for varying flow rates and viscoelasticity. The corresponding match between the pressure drop across the CE slit was less accurate, with the simulation under-predicting the pressures in all three materials, similar to previously reported studies. Simulations performed for the cross-slot geometry found good qualitative agreement with experimental findings, but quantitative discrepancies were found. Subsequent transient comparison in two cases highlighted good qualitative prediction of the PSD development, although discrepancies in the speed of the development were found. These discrepancies may be the result of either the software’s inability to deal with the increased extensional strain in both flows, the three-dimensional nature of the experiments or the failure to fully capture the rheological behaviour of longer relaxation modes in uniaxial extension. Further work will focus on identifying which of these three

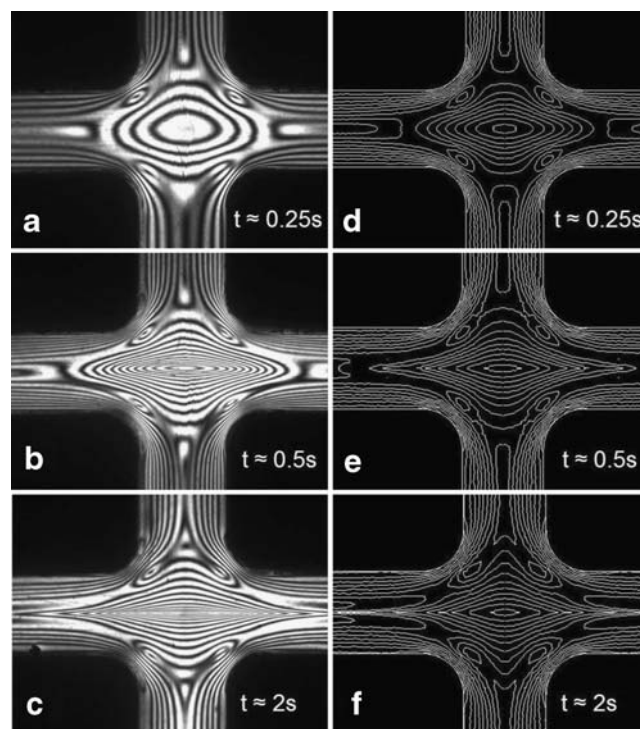


Fig. 12 Transient flow induced birefringence images for HDB2 at a flow rate of $\sim 138 \text{ mm}^3 \text{ s}^{-1}$ per inlet, maximum central extension rate of $\sim 7.6 \text{ s}^{-1}$, highlighting the principal stress difference profile development from initially Newtonian to increasing asymmetry. a–c Experimental results and d–f the corresponding simulation predictions. Direction of the flow (illustrated in Fig. 4) is into the cross-slot through the vertical channels and out through the horizontal ones. As a representation of scale, the cross-slot channel width is 1.5 mm

factors results in these observed differences between simulations and experimental work for this geometry.

Acknowledgements We would like to thank N. Inkson, K. Coventry, S. Butler, O. Harlen, H. Klein and J. Embery for useful input and discussions and Dow for materials. All authors would like to acknowledge funding under the EPSRC MUPP² research project.

References

- Agassant JF, Baaijens F, Bastian H, Bernnat A, Bogaerds ACB, Coupez T, Debbaut B, Gavrus AL, Goublomme A, van Gurp M, Koopmans RJ, Laun HM, Lee K, Nouatin OH, Makley MR, Peters GWM, Rekers G, Verbeeten WHM, Vergnes B, Wagmer MH, Wassner E, Zoetelief WF (2002) The matching of experimental polymer processing flows to viscoelastic numerical simulation. *International Polymer Processing XVII* 1:3–10
- Barakos G, Mitsoulis E (1995) Numerical simulation of extrusion through orifice dies and prediction of Bagley correction for an IUPAC-LDPE melt. *J Rheol* 39(1):193–209
- Bent J, Hutchings LR, Richards RW, Gough T, Spares R, Coates PD, Grillo I, Harlen OG, Read DJ, Graham RS, Likhtman AE, Groves DJ, Nicholson TM, McLeish TCB (2003) Neutron-mapping polymer flow: scattering, flow visualisation and molecular theory. *Science* 301:1691–1695
- Beraudo C, Fortin A, Coupez T, Demay Y, Vergnes B, Agassant JF (1998) A finite element method for computing the flow of multi-mode viscoelastic fluids: comparison with experiments. *J Non-Newtonian Fluid Mech* 75(1):1–23
- Blackwell RJ, Harlen OG, McLeish TCB (2000) Molecular drag-strain coupling in branched polymer melts. *J Rheol* 44:121–136
- Checker N, Mackley MR, Mead DW (1983) On the flow of molten polymer into, within and out of ducts. *Philos Trans R Soc Lond A* 1504(308):451–477
- Clemeur N, Rutgers RPG, Debbaut B (2004a) Numerical simulation of abrupt contraction flows using the double convected pom-pom model. *J Non-Newtonian Fluid Mech* 117:193–209
- Clemeur N, Rutgers RPG, Debbaut B (2004b) Numerical evaluation of three dimensional effects in planar flow birefringence. *J Non-Newtonian Fluid Mech* 123:105–120
- Collis MW, Mackley MR (2005) The melt processing of monodisperse and polydisperse polystyrene melts within a slit entry and exit flow. *J Non-Newtonian Fluid Mech* 128(1):29–41
- Coventry KD (2006) Cross-slot rheology of polymers. PhD Thesis, Department of Chemical Engineering, University of Cambridge
- Coventry KD, Mackley MR (2008) Cross-slot extensional flow of polymer melts using a multi-pass rheometer. *J Rheol* (in press)
- Crowley DG, Frank FC, Mackley MR, Stephenson RG (1976) Localised flow birefringence of polyethylene oxide solutions in a four roll mill. *J Polym Sci* 14:1111–1119
- Das C, Inkson NJ, Read DJ, Kelmanson K (2006) Computational linear rheology of general branch-on-branch polymers. *J Rheol* 50(2):207–234
- den Doelder CF, Koopmans R, Dees M, Mangnus M (2005) Pressure oscillations and periodic extrudate distortions of long-chain branched polyolefins. *J Rheol* 49(1):113–126
- Frank FC, Mackley MR (1976) Localized flow birefringence of polyethylene oxide solutions in a two roll mill. *J Polym Sci A2* (14):1121–1131
- Han CD (1976) *Rheology in polymer processing*. Academic, New York
- Han CD, Drexler LH (1973) Studies of converging flows of viscoelastic polymeric melts. I. Stress–birefringent measurements in the entrance region of a sharp-edged slit die. *J Appl Polymer Sci* 17:2329–2354
- Harlen OG, Rallison JM, Chilcott MD (1990) High-Deborah-number flows of dilute polymer solutions. *J Non-Newtonian Fluid Mech* 34:319–349
- Harlen OG, Hinch EJ, Rallison JM (1992) Birefringent pipes: the steady flow of a dilute polymer solution near a stagnation point. *J Non-Newtonian Fluid Mech* 44:229–265
- Harlen OG, Rallison JM, Szabo P (1995) A split Lagrangian–Eulerian method for simulating transient viscoelastic flows. *J Non-Newtonian Fluid Mech* 60:81
- Hassell DG, Mackley MR (2008) Localised flow induced crystallisation of a polyethylene melt. *Rheol Acta*. DOI 10.1007/s00397-008-0263-6
- Hertel D, von Leon L, Münstedt H (2007) Flow of polyethylene melts into a slit die investigated by laser-Doppler velocimetry. Presentation AERC Naples
- Inkson NJ, McLeish TCB, Harlen OG, Groves DG (1999) Predicting low density polyethylene melt rheology in elongational and shear flows with “pom-pom” constitutive equations. *J Rheol* 43:873–896
- Kiriakidis DG, Park HJ, Mitsoulis E, Vergnes B, Agassant J-F (1993) A study of stress distribution in contraction flows of an LLDPE melt. *J Non-Newtonian Fluid Mech* 47:339–356
- Lee K, Mackley MR, McLeish TCB, Nicholson TM, Harlen O (2001) Experimental observation and numerical simulation of transient stress fangs within flowing molten polyethylene. *J Rheol* 45(6):1261–1277
- Lodge AS (1955) Variation of flow birefringence with stress. *Nature* 176:838
- Luap C, Karlina M, Schweizer T, Venerus DC (2006) Limit of validity of the stress-optical rule from polystyrene melts: influence of polydispersity. *J Non-Newtonian Fluid Mech* 138(2-3):197–203
- Mackley MR, Marshall RTJ, Smeulders JBAF (1995) The multipass rheometer. *J Rheol* 39(6):1293–1309
- Macosko CW (1994) *Rheology, principles, measurements and applications*. Wiley-VCH, New York
- Martyn MT, Groves DJ, Coates PD (2000) In process measurement of apparent extensional viscosity of low density polyethylene melts using flow visualization. *Plast Rubber Compos* 29:14–22
- McLeish TCB, Larson RC (1998) Molecular constitutive equations for a class of branched polymers: the pom-pom polymer. *J Rheol* 42(1):81–110
- Meissner J, Hostettler J (1994) A new elongational rheometer for polymer melts and other highly viscoelastic liquids. *Rheol Acta* 33(1):1–21
- Mitsoulis E, Schwetz M, Münstedt H (2003) Entry flow of LDPE melts in a planar contraction. *J Non-Newtonian Fluid Mech* 111(1):41–61
- Park HJ, Kiriakidis DG, Mitsoulis E, Lee K-J (1992) Birefringence studies in die flows of an HDPE melt. *J Rheol* 36:1563–1583
- Peters GWM, Schoonen JFM, Baaijens FPT, Meijer HEH (1999) On the performance of enhanced constitutive models for polymer melts in a cross-slot flow. *J Non-Newtonian Fluid Mech* 82:387–427
- Schoonen J (1998) Determination of rheological constitutive equations using complex flows. Ph.D. Thesis, Eindhoven University of Technology, downloadable from <http://www.mate.tue.nl>
- Schoonen JFM, Swartjes FHM, Peters GWM, Bjens FPT, Meijer GWM (1998) A 3D numerical/experimental study on a stagnation flow of a polyisobutylene solution. *J Non-Newtonian Fluid Mech* 79(2–3):529–561
- Scrivener O, Berner C, Cressely R, Hocquart R, Sellin R, Vlaches NS (1979) Dynamical behaviour of drag-reducing polymer solutions. *J Non-Newtonian Fluid Mech* 5:475–495
- Sirakov I, Ainsler A, Haouche M, Guillet J (2005) Three-dimensional numerical simulation of viscoelastic contraction flows using the

- Pom-Pom differential constitutive model. *J Non-Newtonian Fluid Mech* 126(2):163–173
- Soulages J (2007) Flow birefringence and velocity measurements for polymer melts in a cross-slot flow channel. Ph.D. Thesis no. 17180. ETH Zürich
- Soulages J, Schweizer T, Venerus DC, Hostettler J, Mettler F, Kroger M, Ottinger HC (2007) Lubricated optical rheometer for the study of two-dimensional complex flows of polymer melts. *J Non-Newtonian Fluid Mech* 150:43–55
- Sridhar T, Tirtaatmadja V, Nguyen DA, Gupta RK (1991) Measurement of extensional viscosity of polymer solutions. *J Non-Newtonian Fluid Mech* 40(3):271–280
- Taylor GI (1934) The formation of emulsions in definable fields of flow. *Proc R Soc Lond A* 146:501–523
- Valette R, Mackley MR, Hernandez Fernandez del Castillo G (2006) Matching time dependent pressure driven flows with a Rolie Poly numerical simulation. *J Non-Newtonian Fluid Mech* 136(2–3):118–125
- Venerus DC, Zhu SH, Öttinger HC (1999) Stress and birefringence measurements during the uniaxial elongation of polystyrene melts. *J Rheol* 43(3):795–813
- Verbeeten WMH (2001) Computational polymer melt rheology. PhD Thesis, Technische Universiteit Eindhoven
- Wagner MH, Rolon-Garrido VH, Chai CK (2005) Exponential shear flow of branched polyethylenes in rotational parallel-plate geometry. *Rheol Acta* 45:164–173
- Wales JLS (1976) The application of flow birefringence to rheological studies of polymer melts. PhD Thesis, Delft University of Technology, Delft
- Wood-Adams P, Costeux S (2001) Thermorheological behaviour of polyethylene: effects of microstructure and long chain branching. *Macromolecules* 34:6281–6290